Chapter – 5

CuO nanoparticles for Enhanced Photoelectrochemical HER Activity

Publication: *Ashish K. Ranjan, Prabhakar Singh, "CuO nanoparticles for enhanced photoelectrochemical HER activity", International Journal of Hydrogen Energy. (Accepted), https://doi.org/10.1016/j.ijhydene.2024.08.302*

CHAPTER 5: CuO nanoparticles for Enhanced Photo-Electrochemical HER Activity

5.1 Introduction

It has already been discussed in Chapter 4 that CuO and self-assembled CuO/Cu_2O heterostructures are promising materials for hydrogen production. We obtained an exceptional amount of H_2 production, which was $\sim 0.59\ \mathrm{kmolh^{-1}g^{-1}}$, using CuO/$Cu_2O$ thin films. Nanostructuring has played an important role in enhanced hydrogen production because it gives more surface area and active sites for the redox reaction. In this chapter, we have synthesized CuO nanoparticles using the hydrothermal technique. These nanoparticles were used as photocathodes in the photoelectrochemical cell to understand HER activity. Photoelectrochemical (PEC) cells that use light from the sun, a renewable energy source, may be addressed to fulfill the rising demand for renewable energy sources [14][229][230]. After the 1973 oil crisis triggered a worldwide quest for alternative energy sources, research into photoelectrochemical cells has undergone intense development. More than a thousand publications have appeared in the space of several years [231]. Since PEC cells combine solar energy collection with water electrolysis, they are extensively employed as devices for solar water splitting. In addition, they spatially segregate the oxygen evolution reaction (OER) and hydrogen evolution reaction (HER). This separation enables the investigation of the kinetics of corresponding half-cell reactions. Multiple strategies have been employed to enhance the PEC performance, such as doping with other metals [232][233], coupling with other semiconductors [234], and optimizing the particle size and morphology [235][236]. These modifications have shown their potential to increase the photocurrent density and improve the overall efficiency of the PEC cell.

Copper oxide (CuO) is considered as a photocathodic material, and it has captured significant interest as a potential material for photoelectrochemical studies for splitting water and hydrogen generation because of its unique properties, such as efficient light harvesting, high hole mobility, and low cost [237][238]. Currently, the most active and stable HER catalyst in commercially available electrolyzers is platinum (Pt) based materials, but their low availability and high costs make it difficult to scale up for practical hydrogen production [239][240]. To replace the highly expensive Pt, transition metal-based materials, such as selenides [241][242], nitrides [243][244], metal sulfides [245][246][247][248][249], carbides [250][251], oxides [252][253] are proposed. Among these, the advantage of CuO photocatalyst lies in its ability to provide an environment-friendly and sustainable way to yield valuable fuels and chemicals. For example, photocatalysis of CuO has been used for the degradation of organic pollutants in water [254][255], the generation of hydrogen through water splitting [256], and the reduction of carbon dioxide [257][258] to methanol in the process where copper oxide (CuO) is used as a catalyst to drive a chemical reaction under the influence of light. There are several copper oxide phases; out of these, cubic cuprous oxide (Cu_2O) and monoclinic cupric oxide (CuO) are the two most stable phases, which possess bandgaps ranges between ∼ 1.4 eV–2.18 eV with many advantageous semiconducting as well as PEC properties [91][238]. Materials with low bandgap energies are favored to develop effective photocathodes because electron-hole pairs can only be produced by the photons having energy above the bandgap. Specifically, CuO photocatalysis involves the absorption of photons by the CuO catalyst, which transfers a valence band electron to the conduction band, creating a pair of electrons and holes. These charge carriers then participate in redox reactions with adsorbed reactant molecules, producing the desired reaction products. This reaction produces oxygen gas, and the electrons from the external circuit are used to reduce protons to hydrogen gas at the photocathode. CuO with lower bandgap energy is among the few photocatalysts with intense activity for photocatalysis of HER under simulated solar radiation, particularly when paired with other photocatalysts [259][260]. However, CuO photocatalysis may be subject to certain limitations because the overpotential of HER at the surface of CuO is relatively high, which affects the majority of semiconductor oxides and is a prevalent issue. The relatively low efficiency of the process, which can be attributed to electron and hole recombination, high overpotential, and insufficient light absorption by the catalyst, is one of the challenges [261]. Additionally, CuO photocatalysis is currently limited to specific reactions and may require optimization of reaction conditions and catalyst design for optimal performance.

In this paper, we report on the facile synthesis of highly crystalline CuO nanoparticles (NPs) by the versatile hydrothermal method. Here, we have investigated the electrochemical performance of CuO NPs for HER by applying solar light and compared them with the dark (no light) condition. We used AM 1.5G solar light to study the PEC performance through three electrode systems in 1 M Na_2SO_4 electrolyte solution with pH ~ 7. The study indicates better PEC performance in the presence of light than performance in the dark. When sunlight irradiates the photocathode, the CuO nanoparticles absorb the photons, generating electron-hole pairs and initiating redox reactions. The generated electrons catalyze the reduction of water molecules, resulting in the formation of H_2. The chronoamperometric result shows the photocathode's stability and relatively short current decay time.

5.2 Experimental Section

5.2.1 Synthesis

For the synthesis of CuO, $Cu(NO_3)_2 \cdot 3\ H_2O$ and NaOH with high purity (> 99%) were used as raw materials bought from Thermo Fisher Scientific. The hydrothermal approach was used to synthesize the CuO NPs, and the process was optimized from the initially reported work [262] to obtain better crystallinity. The hydrothermal reaction was repeated several times for different temperatures and different times in order to get better crystallinity. It was observed that hydrothermal reaction maintained at 188 °C for 96 hours gave the best result. The typical synthesis method involved dissolving cupric nitrate (0.4 M) and NaOH (0.4 M) independently in 40 ml of distilled water and stirring with a magnetic stirrer for 10 minutes. After that, both precursors were mixed and agitated again for 35 minutes at room temperature. Then, the final product was stored in a stainless steel autoclave (Teflon-lined). For the hydrothermal reaction, the temperature was maintained at 188 °C for 96 hours. Following the synthesis procedure, the obtained residual dispersion was washed many times using distilled water until the pH of the solution reached ~7. The sample obtained was filtered and dried in a hot air oven at 100 °C for 1 hr. The obtained NPs were calcined at 700 °C for 1 hr to remove the unwanted species.

5.2.2 Material Characterization

X-ray diffraction (XRD) technique was employed using a Rigaku miniflex II diffractometer with CuKα radiation to ascertain the phase and crystal structure of the sample at room temperature. Further, the Rietveld refinement also verified the structure of the synthesized sample. To visualize the structural morphology and estimate the average size of particles of the NPs, high-resolution scanning electron microscopy (HR-SEM), high-resolution transmission electron microscopy (HR-TEM), and selected area electron diffraction (SAED) measurements were conducted using Nova Nano SEM 450, and TECNAI G^2 20 200kV TEM (FEI) respectively. The Energy-dispersive X-ray analysis (EDAX) spectrum was obtained using EDAX Pegasus integrated EDS-EBSD (EDAX Inc.) The optical absorbance spectrum was recorded using a JASCO V-770 UV spectrometer. The X-ray photoelectron spectroscopy (XPS) was measured using Thermo Fisher Scientific (Kα model). The photocatalytic cyclic voltammetry (CV), linear sweep voltammetry (LSV), and chronoamperometry were recorded through a Keithley 2450 source meter using the three-electrode measurement setup. A 1 M sodium sulfate solution (Na_2SO_4) was prepared for the electrolyte. A reference electrode consisting of Ag/AgCl stored in a 1 M KCl (potassium chloride) solution and a counter electrode of Pt wire was used in the measurement. CV measurements were performed at the scan rates of 50, 100, 150, and 200 mV/s using CuO NPs as a working electrode. A solar simulator (Sciencetech class AAA, AM 1.5G) with a Xenon arc lamp having an intensity of 1000 W/cm^2 is used as a light source.

5.3 Results and Discussion

5.3.1 Structural Study

The X-ray diffractograms were analyzed for the structural examination of CuO NPs. The diffraction peaks before the sample is calcined (with impurity) are shown in Fig. 5.1(a). The temperature and time were optimized in many steps, i.e., we calcined the samples at 650 °C, 700 °C and 750 °C and found that at the calcination temperature of 700 °C, no unwanted phase was obtained, as shown in Fig. 5.1(b). The temperature of 700 °C was selected to obtain the required phase crystallinity and avoid excess grain growth and agglomeration, which could alter the size and surface area of the NPs. After calcination, we observed that CuO NPs were crystalline with no impurities. The analysis indicates that every diffraction peak found in the sample fits the standard data (JCPDS card no. 895895) quite well and can be indexed to a monoclinic phase with space group C2/c (HM #15). Corresponding cell parameters are obtained as; a = 4.681 Å, b = 3.423 Å, and c = 5.126 Å with α = γ = 90°, β = 99.42°. The full width at the half-maximum (FWHM) value was obtained as 0.3128 radians, and the corresponding average crystallite size calculated from the most intense peak at 2θ = 38.84 using the Debye - Scherer relation [263] is found to be 28 nm.

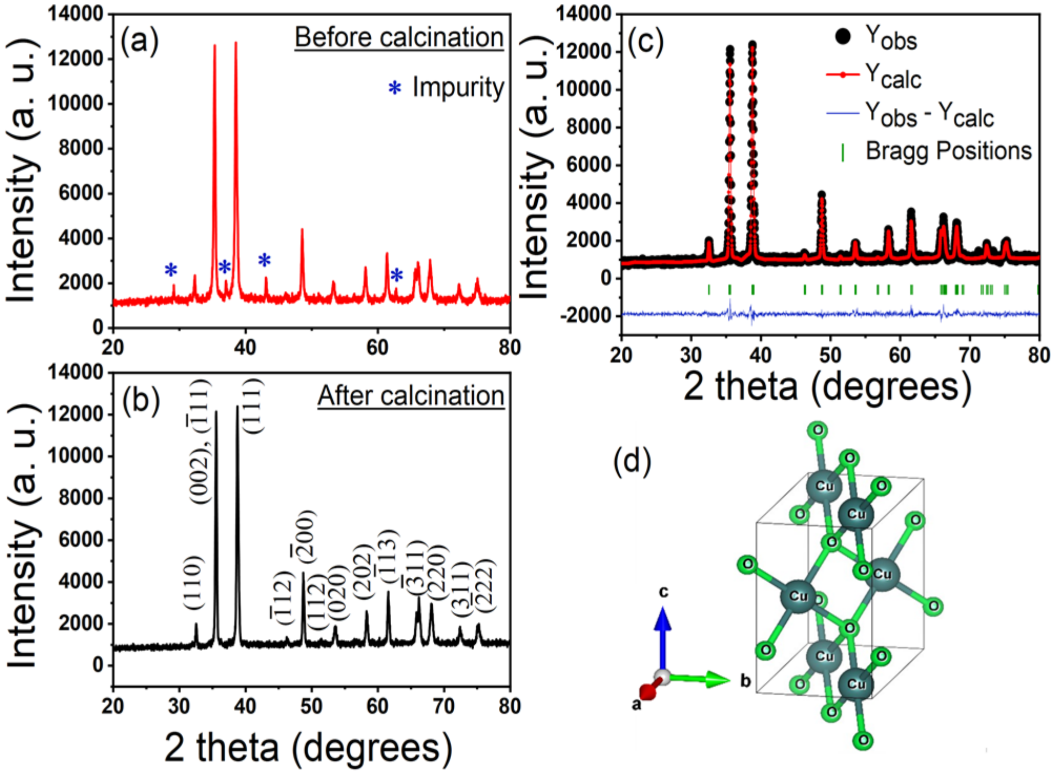

Figure 5.1: X-ray diffractograms (a) Before calcination (b) After calcination, (c) Rietveld refinement, and (d) Crystal structure of CuO NPs.

Rietveld refinement of XRD data, as shown in Fig. 5.1(c), also affirms the monoclinic phase of CuO NPs. Moreover, it can be seen from the figure that Y_{calc} data almost converges with

Y_{obs} data. The obtained R-factors, such as the weighted profile residual factor (R_{wp}), the expected residual factor (R_{exp}), and the reduced χ^2 parameters, were extracted to examine the quality of the refinement. The final values of R_{wp}, R_{exp}, and χ^2 are determined as 19.4, 8.52, and 5.18, respectively, suggesting a good correlation with the experimental results. Fig. 5.1(d) shows the generated crystal structure of CuO NPs obtained from the Rietveld refinement data and labeled with Cu and O atomic positions.

5.3.2 Thermogravimetric Analysis (TGA)

TGA analysis was used to estimate the calcined nanopowder's mass loss and thermal stability under the N_2 atmosphere, with temperature ranging from room to 1000 °C, as shown in Fig. 5.2. From the curve, it can be observed that the sample undergoes a gradual mass loss followed by three steps of decomposition.

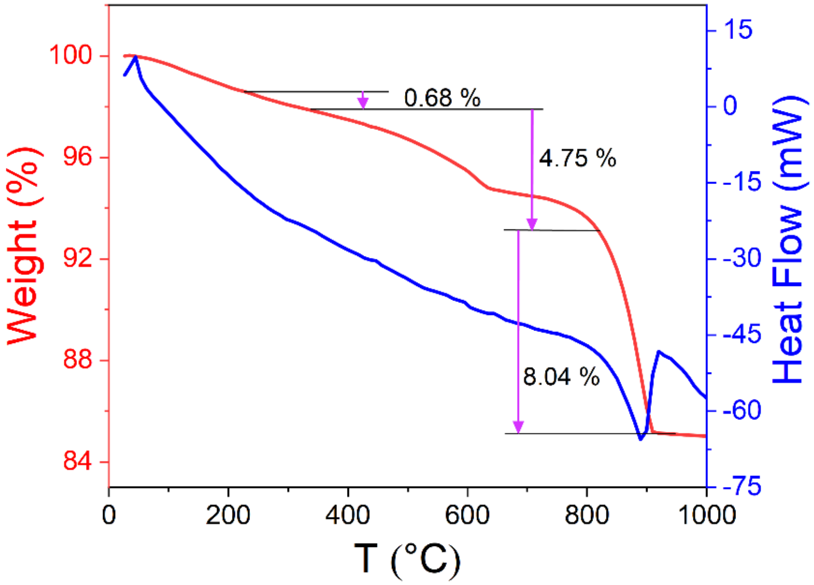

Figure 5.2: TGA and DSC curves illustrating stepwise mass loss and thermal decomposition.

The first decomposition of 0.68 % occurs between the temperature range 227 - 335 °C, which is related to the removal of moisture from the sample; the second decomposition of 4.75 % occurs between 335 - 815 °C, which is associated with the decomposition of nitrate compounds, and the third decomposition of 8.04 % occurs between 815 - 913 °C can be attributed to oxygen vacancy.

According to the plot, the total observed weight loss of CuO nanoparticles is 13.47 %. We have also plotted differential scanning calorimetry (DSC) data (Fig. 5.2) to get quantitative information about exothermic and endothermic processes. The endothermic peak at ~ 900 °C indicates CuO's melting process and thermal decomposition [264].

5.3.3 HR-SEM and HR-TEM Analysis

A HR-SEM micrograph of CuO NPs depicting the surface morphology is shown in Fig. 5.3(a). The image confirms the formation of NPs with the average particle size ranging from 30 - 35 nm. The inset plot in Fig. 5.3(a) shows the bar chart and grain size distribution of the CuO NPs, where the average grain size was estimated to be ~ 26 nm. The Energy-dispersive X-ray analysis (EDAX) result shown in Fig. 5.3(b) affirms the presence of Cu and O only, which indicates the sample is impurities-free. The Cu and O atomic percentages are 58.22 % and 41.78 %, respectively, suggesting that synthesized CuO NPs appear slightly Cu-rich. TEM analysis is one of the more sophisticated nano-characterization techniques for determining optimal morphologic properties and crystal quality of as-grown CuO nanoparticles. The HR-TEM and SAED images are investigated to thoroughly understand the synthesized nanoparticles. The TEM image shown in Fig. 5.3(c) indicates the CuO NPs agglomeration with cubic and quasi-spherical structures of individual particles. The observed diameter of the nanoparticles ranges from approximately 20 to 40 nm. The estimated mean particle size of the

NPs is ~ 34 nm. The corresponding SAED pattern in Fig. 5.3(d) shows the ring-like pattern affirming the crystalline nature of the synthesized CuO NPs. The SAED patterns are indexed to the monoclinic phase of CuO and agree with the XRD results. The plane (111) corresponds to the 2θ = 38.67° (major peak), and (-311) corresponds to 66.19° of CuO.

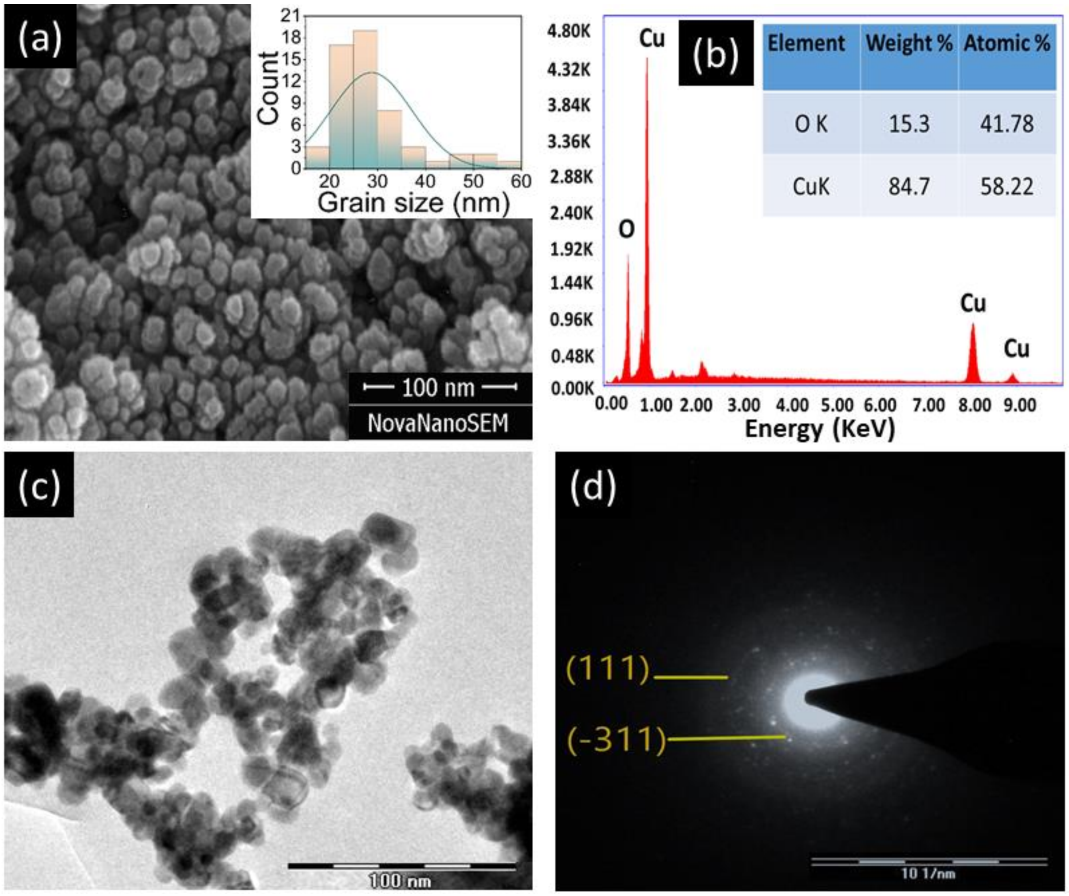

Element	Weight %	Atomic %
O K	15.3	41.78
CuK	84.7	58.22

Figure 5.3: Depicts (a). FESEM micrograph with grain size distribution in the inset (a), (b) EDAX spectra, (c) Transmission electron microscopy image at 100 nm resolution, and (d) SAED image of CuO NPs.

5.3.4 Optical Studies of CuO NPs

To understand the optical absorption behavior of CuO NPs, the UV-visible spectra are plotted between the wavelength range 300 – 1200 nm. The absorbance properties of CuO NPs are also essential when we use them as a photocatalyst for PEC HER because they are directly related to the absorption of photons and generating electron-hole pairs in the electrolyte solution [257]. Here, a broad absorbance spectrum up to 800 nm is observed, and a peak at nearly 609 nm is obtained, as shown in Fig. 5.4(a). Further, the optical bandgap has been estimated from Tauc's plot, as shown in Fig. 5.4(b), using the relation [118][119] given by equation 5.1.

$$(\alpha h\nu)^2 = A\left(h\nu - E_g\right) , \tag{5.1}$$

where A is the absorbance, hν is the incident photon's energy, α is the absorption coefficient, and E_g is the bandgap. A bandgap of 1.37 eV is obtained, which agrees with the previously reported bandgap of CuO (bulk and thin films) [63][89][90]. Due to the narrow bandgap, there is a possibility of photogenerated electron-hole pair recombination. Several factors that prevent the recombination, such as (a) nanostructuring the CuO can increase the surface area, improve light absorption, and enhance the generation of electron-hole pairs and minimize the recombination; (b) proper band alignment minimizes the energy losses and reduce the recombination.

Urbach tail is associated with defects in the molecule, which are led by structural disorder. These defects prevent the direct transition of irradiated electrons from the valance band to the conduction band by trapping them. In the absorption spectra, these defect states generate an absorption tail (see Fig. 5.4(d)). This particular absorption tail is also called the Urbach tail, and the connected energy is called Urbach Energy [120]. The equation used to calculate the Urbach energy is as follows:

$$\mathrm{\alpha} = \mathrm{\alpha}_0 \exp\left(\frac{\mathrm{E}}{\mathrm{E_U}}\right)$$

$$\text{or,}\quad \ln \alpha = \ln \alpha_0 + \left(\frac{E}{E_U}\right), \tag{5.2}$$

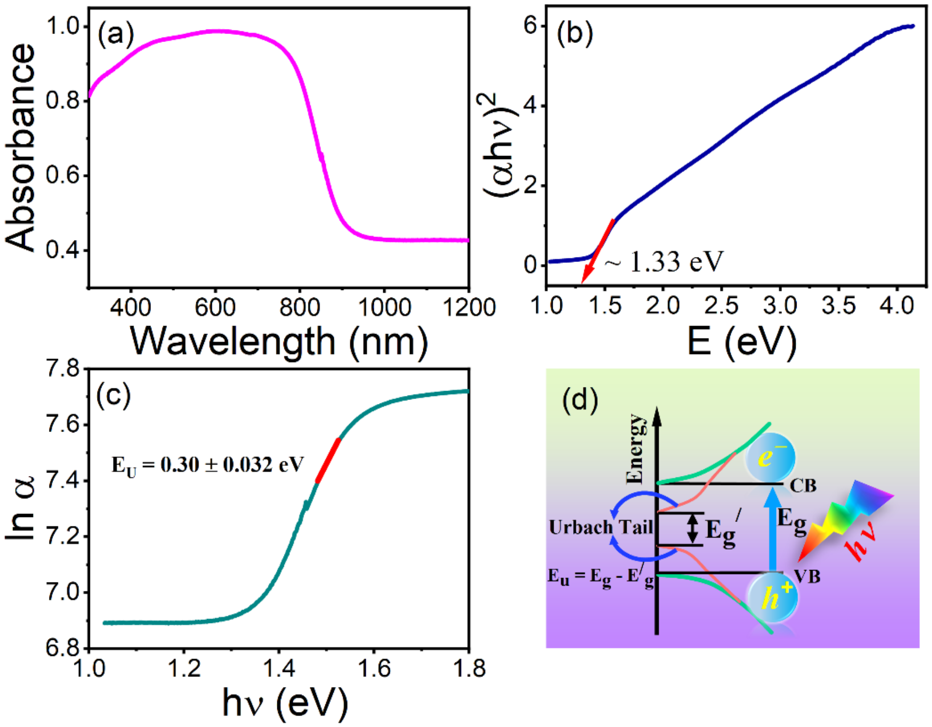

Figure 5.4: Depicts the Tauc plot, Inset (a) absorbance spectrum between 300 – 1200 nm, Inset (b) Urbach energy plot of the CuO nanoparticles, and (c) schematic of the bandgap and Urbach tail between the valence band (VB) and the conduction band (CB).

where E is the incident photon's energy, and E_U is Urbach energy. E_U can be calculated by linearly fitting the plot of ln (α) versus E and taking the reciprocal of the slope as shown in Fig. 5.4(c). The obtained Urbach energy of CuO NPs is ~ 0.30 ± 0.032 eV, indicating a moderate degree of structural disorder in the material [265], which is advantageous for HER. This degree of disorder is favorably correlated as it contributes to creating active sites and enhances the PEC performance, such as high photocurrent density and favorable onset potentials [266][267].

5.3.5 XPS Analysis

XPS is an effective and surface-sensitive characterization technique to confirm the material's elemental composition, oxidation state, and purity. A monochromatic source of Al Kα radiation providing a photon energy of 1486.6 eV was employed for the measurement. The C 1s peak at 284.8 eV, shown in Fig. 5.5(d), was used as a calibration reference to measure all the binding energies. The broad XPS spectra, as shown in Fig. 5.5(a), confirm the presence of peaks corresponding to copper (Cu), oxygen (O), and carbon (C) in CuO NPs. The inset plot in Fig. 5.5(a) shows the Valence Band Maximum (VBM), which is nearly 0.67 eV. The work function of CuO calculated from UPS spectra is ~ 4.7 – 5.5 eV, as reported by Zhang, Jun, et al. [268], which is higher than VBM. The high-resolution energy scans of Cu 2p in Fig. 5.5(b) show two major peaks at the binding energies of 933.91 eV and 953.87 eV, corresponding to Cu $2p_{3/2}$ and Cu $2p_{1/2}$ of CuO NPs [269][270].

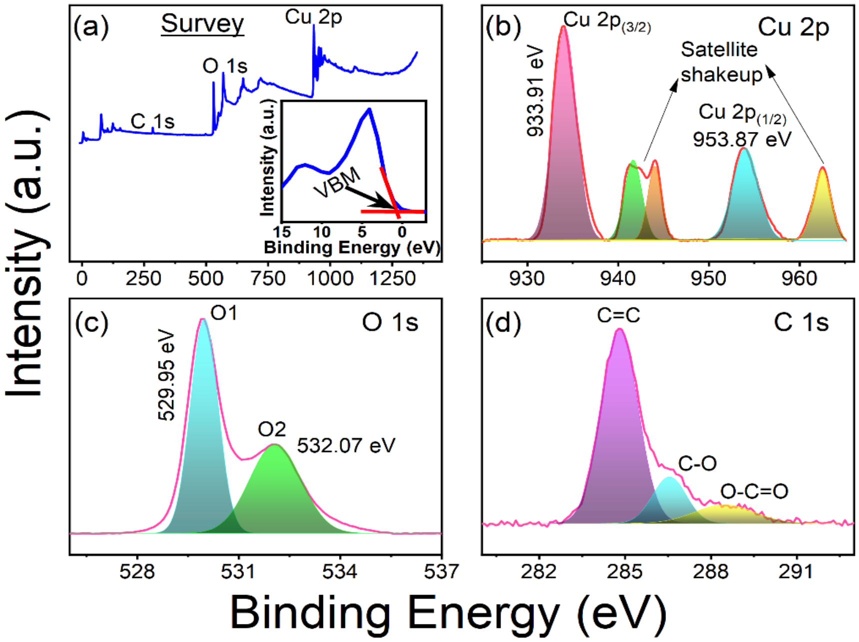

Figure 5.5: (a) Depicts the XPS spectra, core level XPS spectra of (b) Cu 2p, (c) O 1s, and (d) C 1s of CuO nanoparticles.

CuO can be distinguished from metallic Cu and Cu_2O due to the appearance of a strong shake-up peak at a high binding energy side of the Cu $2p_{3/2}$ primary peak and the increase in the primary peak's binding energy suggest the existence of an unfilled $Cu3d^9$ shell and further confirm the presence of Cu^{2+} in the nanoparticles [271]. Fig. 5.5(c) shows the deconvoluted high-resolution XPS spectra of O 1s in the CuO NPs. The most intense peak (denoted as O1) at 529.95 eV can be assigned to O^{2-}, whereas the subsequent peak (O2) at 532.07 eV can be attributed to adsorbed residual carbon or other surface-bound oxygen species [272]. It is evident from XPS spectra that the synthesized CuO NPs are pure and align with our XRD results.

5.3.6 Photoelectrochemical Studies of CuO NPs

The unique properties of CuO nanoparticles make them suitable for photocathodic applications. The photoelectrochemical properties of CuO NPs for HER were measured using three–electrode arrangements in 1 M Na_2SO_4 solution within a potential window (-1.5 to 1.5V) under continuous solar light illumination and dark conditions. The CV curves shown in Fig. 5.6 at the scan rates of 50, 100, 150, and 200 mV/s depict peaks at the cathodic and anodic sweeps, representing the reversible nature of the electrode [84].

It is evident from the plot that the current density (J) is increasing in the light condition compared to the dark condition at all the scan rates. However, the difference in current density under dark and light is not huge, possibly due to the high catalytic efficiency in dark conditions. Further, the peak splitting (both anodic and cathodic) at 100 mV/s indicates multiple redox processes in the system.

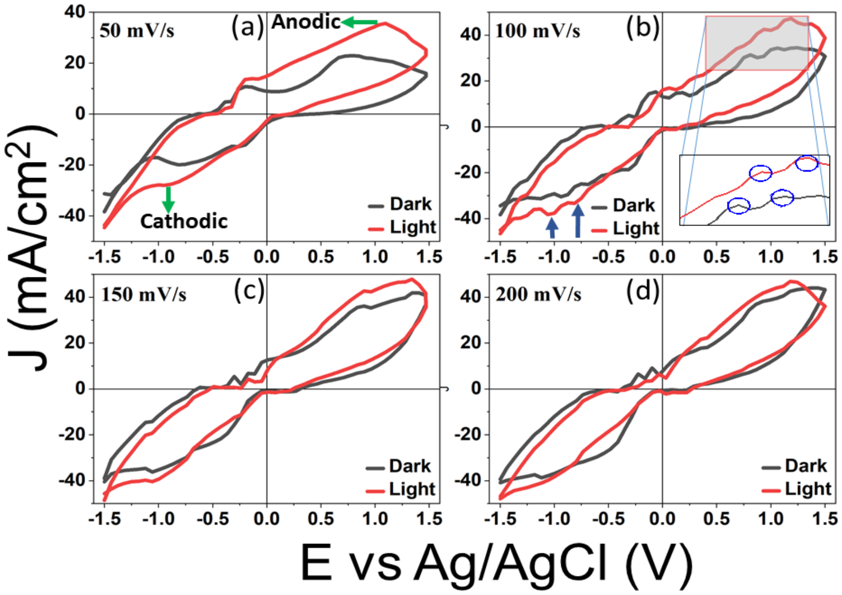

Figure 5.6: Depicts the CV plots of CuO NPs at different scan rates.

In Fig. 5.6(b), the first anodic peak represents the species oxidation at the electrode's surface. The species undergo oxidation and lose electrons, increasing the anodic current when the potential is swept in the positive direction. The concentration of the oxidizable species and electrochemical reactivity are directly related to peak current intensity. The second anodic peak represents different redox processes occurring at the electrode surface. Similarly, the first cathodic peak occurred due to the reduction of the oxidized species, which was generated during the first anodic peak. In contrast, the second cathodic peak was caused by the reduction of the oxidized species produced during the second anodic peak.

The multiple anodic and cathodic peaks present in a CV curve suggest the involvement of numerous electrochemical processes. The anodic (J_{PA}) and cathodic peak (J_{PC}) current density, along with peak-to-peak separation (ΔE_p) in dark and light conditions, are shown in Table 5.1. It is observed that the peak current density increases with the increase in the scan rate as well as in the light condition because the rate of diffusion is greater than that of reaction at higher scan rates. Therefore, more electrolytic ions have reached the electrolyte interface of an electrode, whereas very few are participating in a charge transfer reaction.

Table 5.1 Voltammetric parameters of CuO NPs in dark and light conditions.

Scan Rate mV/s	J_{PA} (mA/cm^2) (Dark)	J_{PA} (mA/cm^2) (Light)	J_{PC} (mA/cm^2) (Dark)	J_{PC} (mA/cm^2) (Light)	J_{corr} (mA/cm^2) (Dark)	ΔE_p (mV) (Dark)	J_{corr} (mA/cm^2) (Light)	ΔE_p (mV) (Light)
50	22.89	35.57	-19.83	-27.92	0.32×10^{-3}	31	1.0×10^{-3}	154
100	31.44	45.26	-29.49	-33.41	0.79×10^{-3}	63	1.12×10^{-3}	234
150	37.01	42.75	-36.2	-40.40	6.11×10^{-3}	128	3.68×10^{-3}	128
200	42.26	46.97	-38.76	-41.04	4.91×10^{-3}	27	5.45×10^{-3}	63

According to the literature [84], the value of ΔE_p in reversible photoelectrochemical processes should be ≤ 59 mV. In addition, this value corresponds to the theoretical limit known as Nernstian behavior, where the barrier for electron transfer is low in a reversible process and high in an irreversible process [84]. However, relying solely on one parameter, i.e., ΔE_p is not suitable for confirming the reversibility or irreversibility of the photoelectrochemical process but also by the reaction kinetics and electrode properties. In an electrochemical reversible electron transfer process, which includes free diffusing redox species, the Randles-Sevcik (RS) equation elucidates the relation of the peak current i_p (A) on the square root of the scan rate (ν) [84].

$$i_p = 0.446\ nFAC^0 \left(\frac{nF\nu D_0}{RT}\right)^{1/2} \tag{5.3}$$

where n is the number of electrons engaged in the redox process, A denotes the electrode surface area, C^0 is the bulk concentration, D_0 stands for the diffusion coefficient, R is the gas constant, T is the absolute temperature, F is the Faraday constant, and ν is the scan rate. The electrode surface area (A) exposed to the electrolyte solution and light is 1.17 cm^2. To understand the peak behavior of CuO NPs, the J_p is plotted against the square root of the scan rate in both dark and solar light conditions, as shown in Fig. 5.7. The plot represents the oxidation (O) and reduction (R) current density peaks, which are almost linear in the dark as well as in light, suggesting a diffusion-controlled mechanism and quasi-electrochemical reversibility. In this case, the diffusion of reactants to the surface of the electrodes is a decisive factor limiting the rate of electrochemical reaction.

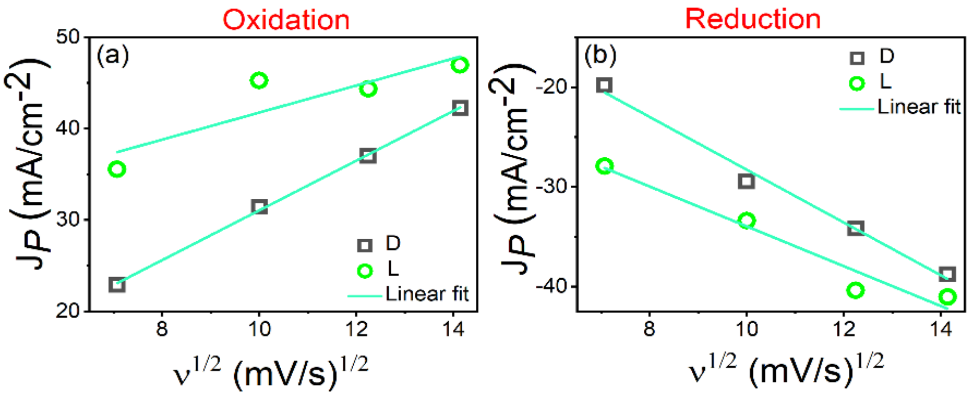

Figure 5.7: R-S equation fitting in dark and light conditions for (a) oxidation and (b) reduction regions of CuO NPs.

The Tafel plot provides information about the corrosion behavior of the material as it relates the polarization (i.e., change in electrode potential) to the corrosion current density (J_{corr}). Figure 5.8 shows the E vs Ag/AgCl variation with logarithmic current density (log J) in light conditions. The same is shown in the dark condition in Fig. 5.9.

In Fig. 5.10(a), J_{corr} is plotted against the scan rate in both dark and light conditions, and it is evident that Jcorr increases with the scan rate under light exposure. This increase in J_{corr} under light exposure may be due to photocorrosion phenomena [273]. A decrease in the J_{corr} indicates a low corrosion rate (CR), indicating the material's lower vulnerability to corrosion.

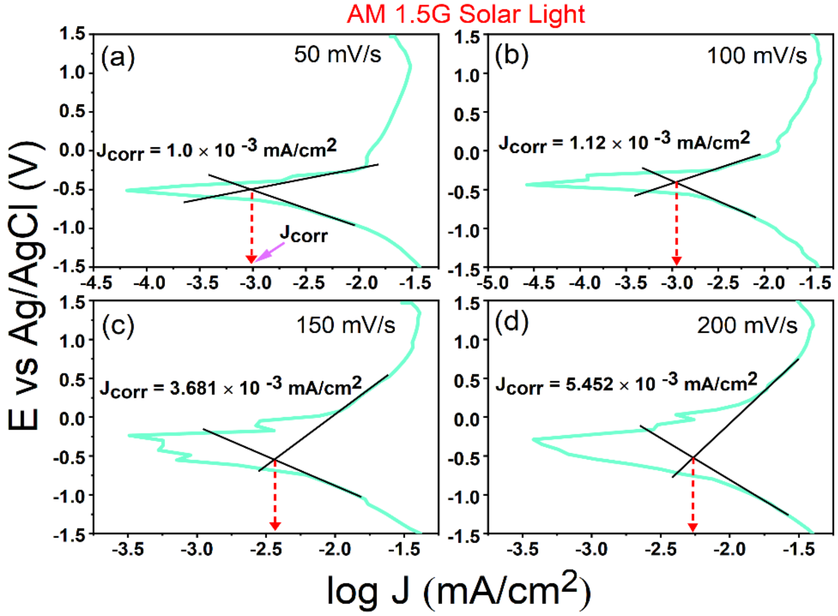

Figure 5.8: Potentiodynamic polarization curves representing J_{corr} of CuO NPs in light conditions.

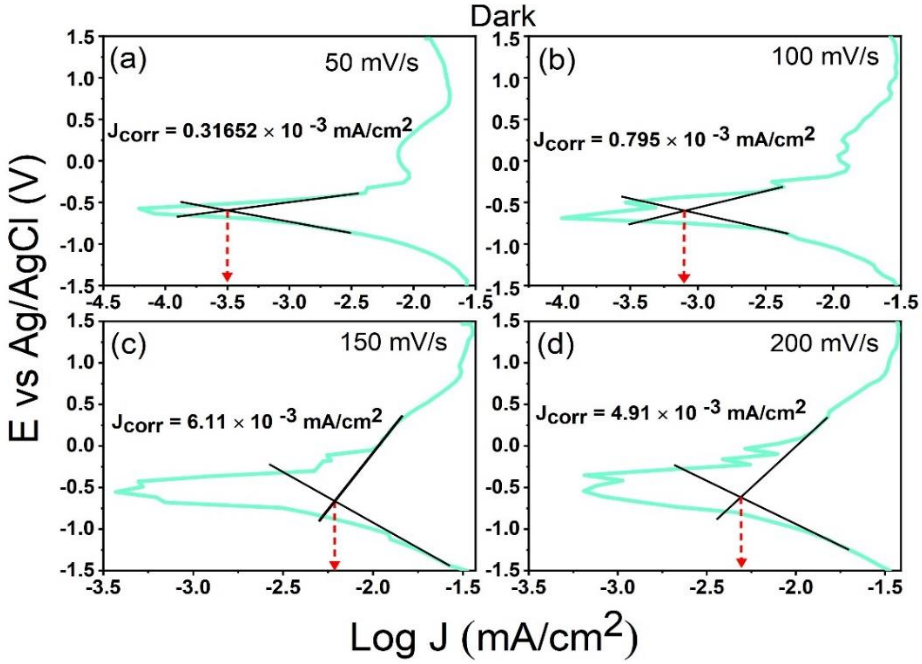

Figure 5.9: Potentiodynamic polarization curves representing J_{corr} of CuO NPs in Dark conditions.

The J_{corr} values obtained from the Tafel plot in dark and light conditions are mentioned in Table 5.1. Interestingly, we observed a very low maximum corrosion current density of 6.11×10^{-3} mA/cm^2 in dark conditions at 150 mV/s as compared to the J_{corr} reported by D. Devadoss et al., 2023 [274], which can be attributed to the higher electrochemical stability of CuO against corrosion.

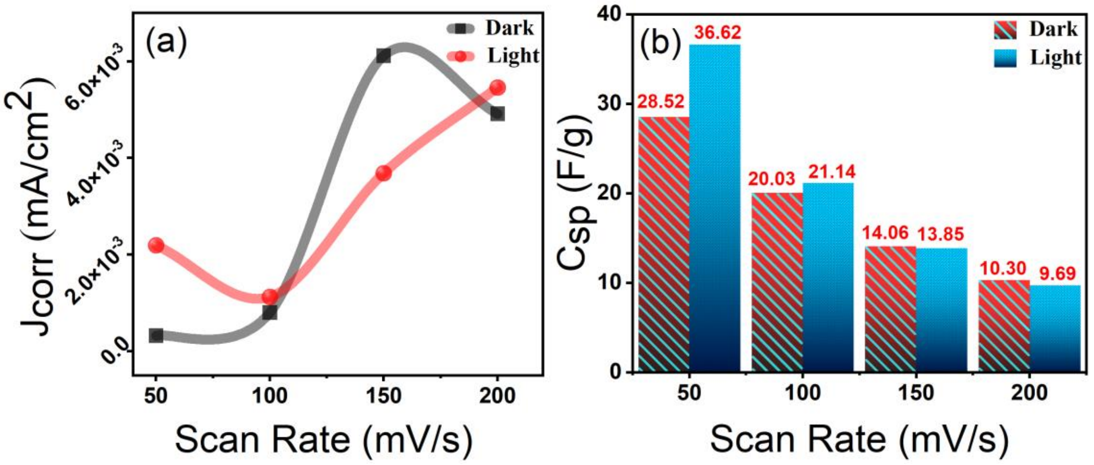

Figure 5.10: (a) Variation of corrosion current density with the scan rate, and (b) specific capacitance bar chart of CuO NPs.

The bar chart in Fig. 5.10(b) shows the specific capacitance (C_{sp}) variation with the scan rate of CuO NPs at different illumination conditions. The C_{sp} of the sample was estimated using the following equation 5.4,

$$C_{sp} = \frac{\int I(V)dV}{m\nu\Delta V} \tag{5.4}$$

where $\int I(V)dV$, m, ν, and ΔV represent the integrated area under the CV curve, the mass of the electrode sample, the scan rate, and the potential window, respectively [275][276]. The sample has shown a significant increase in their C_{sp} under light illumination at low scan rates. However, at higher scan rates, the C_{sp} values in dark and light are observed to be almost the same. Clearly, it can be observed from the bar chart that the C_{sp} is decreasing while increasing the scan rate, which may be due to inadequate diffusion time for electrolyte ions toward the electrode material [277]. All the obtained CV curves (see Fig. 5.6) exhibited a pair of redox peaks (cathodic and anodic), signifying the pseudocapacitive characteristics of CuO NPs. Further, a meticulously curated comparison chart of previously reported specific capacitance of CuO with different morphologies has been shown in Table 5.2 and compared with our data. It was found that the Csp values of CuO NPs were slightly low. Several factors affect the specific capacitance, such as choice of electrolyte, scan rate, absolute surface area, and morphology.

Table 5.2 Comparison chart of specific capacitance of various reported CuO photocathodes with different morphology and synthesis techniques.

Electrode configuration	Electrolyte	Methods	Specific capacitance (F/g)	References
CuO thin film	1 M Na_2SO_4	Chemical bath deposition	60 at 100 mV/s	[278]
CuO-PAA thin film	1 M H_2SO_4	Polymer assisted deposition	65 at 20 mV/s	[279]
CuO-glycine nanoparticles	6 M KOH	Solution combustion synthesis	7.55 at 50 mV/s	[280]
$Ni(OH)_2$/CuO nanocomposite thin films	1 M KOH	SILAR	27 at 10 mV/s	[281]
CuO thin film	1 M Na_2SO_4	Potentiostatic electrodeposition	36 at 20 mV/s	[282]
CuO nanoflakes films	1 M KOH	Surface oxidation	190 at 2 mA	[283]
CuO nanoparticles	1 M Na_2SO_4	Hydrothermal synthesis	36.62 at 50 mV/s	This work

5.3.7 Mott – Schottky Plot Analysis

To elucidate the crucial semiconductor properties of the photocathode, such as the nature of the semiconductor and the flat band potential (V_{fb}), Mott – Schottky (MS) analysis was employed. It is a well-established method that provides valuable insights into charge carrier behavior at the semiconductor-electrolyte interface.

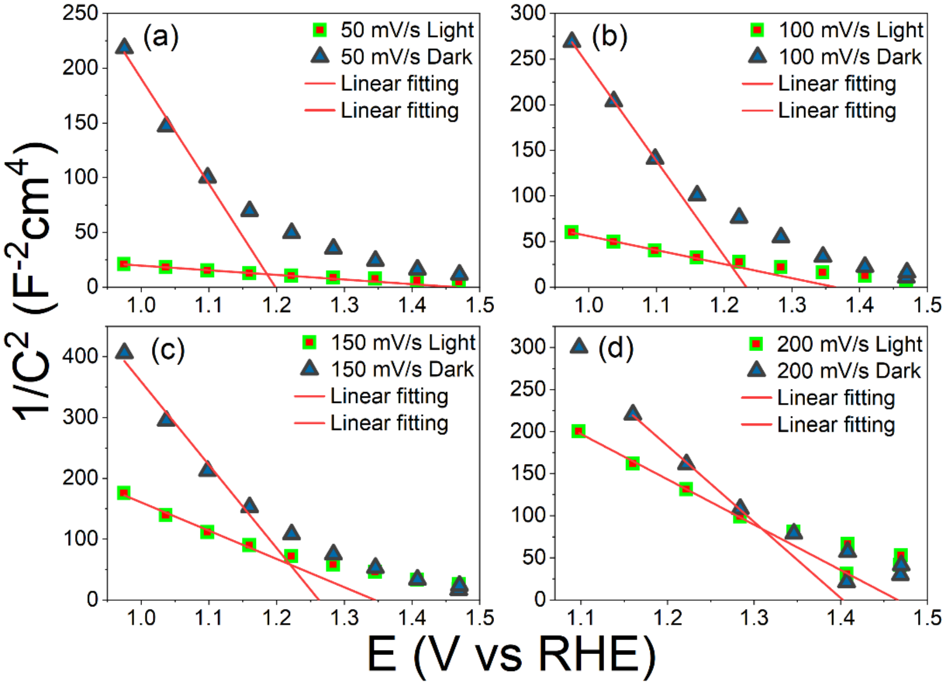

Figure 5.11: Depicts the Mott – Schottky fitting at different scan rates in dark and light conditions.

The Mott – Schottky equation [284][36] that controls the band bending can be stated in the following equation 5.5.

$$\frac{1}{C^2} = \frac{2}{e\varepsilon\varepsilon_0 A^2 N_D}\left(V - V_{fb} - \frac{k_B T}{e}\right) \tag{5.5}$$

where N_D is carrier density, ε is the dielectric constant, ε_0 is permittivity in a vacuum, k_B is Boltzmann's constant, A is the area, T is absolute temperature, e is the electron charge, and V is the applied voltage. The negative slope of all the MS plots shown in Fig. 5.11 suggests the p-type nature of CuO NPs [285]. Further, the V_{fb} is determined from the intercept with the x-axis of the linear portion of the MS plot. The obtained values of V_{fb} are 1.19, 1.22, 1.26, and 1.40 in the dark and 1.46, 1.36, 1.34, and 1.46 V in light conditions at the scan rate of 50, 100, 150, and 200 mV/s, respectively.

5.3.8 HER Activity in CuO Photocathode

The HER generally uses a multi-step reaction mechanism involving proton adsorption, electron transfer, and hydrogen gas formation. The following reactions are used to describe the HER through CuO NPs,

Photon absorption and charge (electron and holes) generation [15]:

$$\mathrm{CuO + h\nu \rightarrow CuO^{*}\,(e^{-} + h)} \tag{5.6}$$

Now, these electrons migrate to the counter electrode and reduce the H^+ ions present in the electrolyte, formed from the dissociation of water molecules, to generate hydrogen gas [286].

$$\mathrm{2H^{+} + 2e^{-} \rightarrow H_2 \uparrow} \tag{5.7}$$

Fig. 5.12(a) shows the cathodic half-cell reaction of the CuO photocathode in light and dark conditions. The measured potentials versus Ag/AgCl were converted to the Reversible Hydrogen Electrode (RHE) using the equation, $E_{RHE} = E_{Ag/AgCl} + E^{0}_{Ag/AgCl} + 0.059\,\mathrm{pH}$, where $E_{Ag/AgCl}$ represents the experimental potential measured against the Ag/AgCl reference electrode, $E^{0}_{Ag/AgCl}$ represents the standard potential of the Ag/AgCl electrode at 25° C and E_{RHE} stands for converted potential versus RHE. Here, we can clearly see the difference in the photocurrent obtained in the light and dark conditions at different scan rates.

Further, Fig. 5.12(a) shows the cathodic half-cell reaction from which the surface charge density (σ) is calculated using the equation($\sigma = \frac{Q}{A}$), where Q is the total charge accumulated at the electrode-electrolyte interface, and A is the surface area of the electrode. The calculated values of σ are 0.052, 0.082, 0.090, 0.093 C/cm^2 in the dark and 0.066, 0.079, 0.080, 0.074 C/cm^2 in light conditions at the scan rate of 50, 100, 150 and 200 mV/s respectively. From the linear sweep voltammetry (LSV) curve, the current density (J) is plotted against the potential (V vs. RHE) of the CuO photocathode in both dark and light conditions, as shown in Fig. 5.12(b).

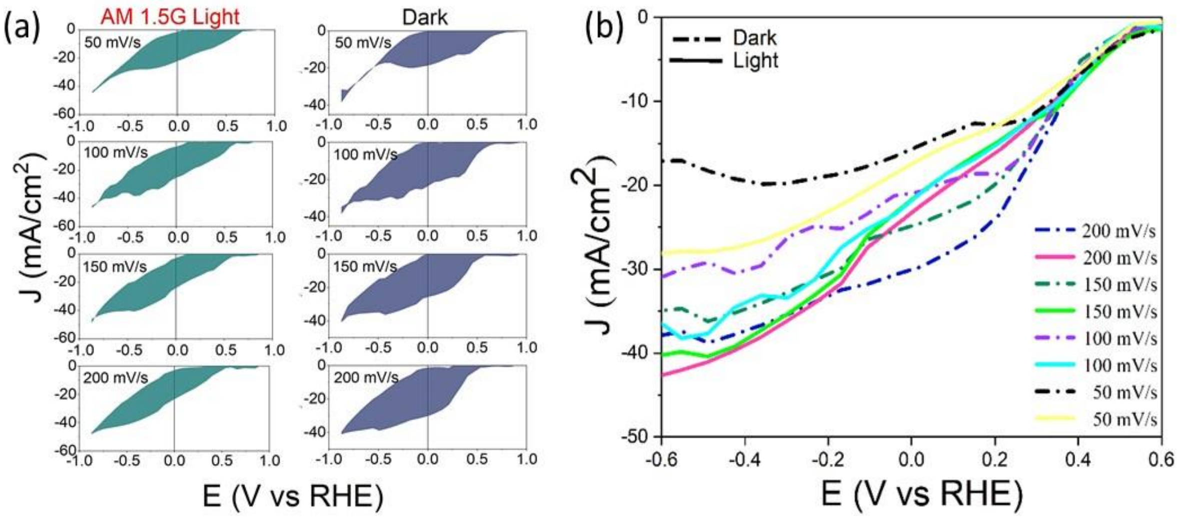

Figure 5.12: (a) Depicts the PEC current density – voltage measurements in the cathodic region at different scan rates, and (b) cathodic J – E curves in dark and light, revealing maximum photocurrent density at -0.6 V vs. RHE.

A remarkable maximum photocurrent density of -41.57 mA/cm^2 is obtained at -0.6 V versus RHE under 1000 W/m^2 light illumination. The onset potential (V_{onset}) at which the CuO NPs catalyze HER is ~ 0.535 V vs. RHE. Further, a comparison chart of previously published photocurrent density of various photocathodes for HER activity is curated and is listed in Table 5.3.

Table 5.3 Comparison chart of photocurrent density of various reported photocathodes with this work.

Photocathode Type and morphology	Precursor used	Fabrication Methods	Photocurrent Density (mA/cm^2)	References
CuO NPs	Cu target	Reactive DC sputtered, and RTP	-6.4 mA/cm^2 at 0.3 V vs. RHE	[287]
CuO Nanostructured	Cu foil (99.5 % pure)	Chemical bath deposition	-1.3 mA/cm^2 at 0 V vs. RHE	[39]
CuO/ZnO nanowire	$Cu(OH)_2$	Electrodeposition of Cu film after chemical oxidation and dip-coating	-8.1 mA/cm^2 at 0 V vs. RHE	[288]
MoS_2 – WS_2/Si	$(NH_4)_2MoS_4$ and $(NH_4)_2WS_4$	Solution casting and subsequent annealing	-25.9 mA/cm^2 at 0 V vs. RHE	[289]
CuO NPs	CuO target	RF-magnetron sputter	-3.1 mA/cm^2 at 0 V vs. RHE	[156]
CuO thin films	CuO target	RF-magnetron sputter	-2.5 mA/cm^2 at 0.5 V vs. RHE	[290]
CuO nano leaf	$CuCl_2 . 2H_2O$	Aqueous solution under a mild refluxing environment	-6.0 mA/cm^2 at -0.2 V vs. RHE	[238]
Mo-doped CuO	Cu and Mo targets	RF sputtering	-2.25 mA/cm^2 at -0.387 V vs. RHE	[291]
CuO NPs	Copper (II) sulfate	Spin coating/Spinning disk reaction	-1.58 mA/cm^2 at 0.5 V vs. RHE	[292]
CuO NPs	Copper (II) nitrate	Hydrothermal synthesis	-41.57 mA/cm^2 at -0.6 V vs. RHE	This work

5.3.9 Transient Current Kinetics via Chronoamperometry

To understand the transient current dynamics that clarify the dynamic nature of electrochemical reactions at the electrode-electrolyte interface, chronoamperometric $(J-t)$ investigations are carried out at a fixed positive potential of 2.63 V vs. RHE under continuous light illumination and in dark conditions within a time range of 0 to 4000 s in which variation of current density is measured with time. The chronoamperometric responses are fitted with a non-linear exponential decay to determine the transient current decay time (τ) (see Fig. 5.13).

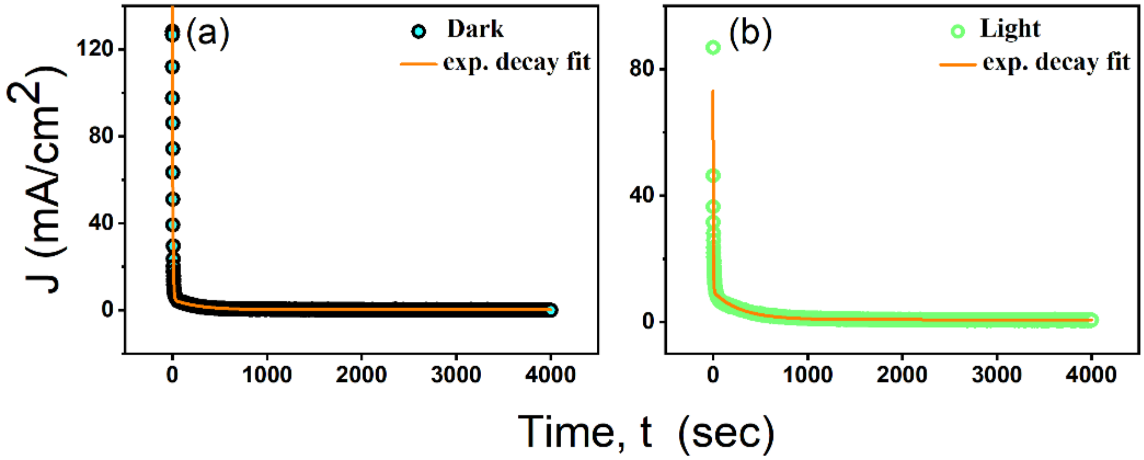

Figure 5.13: Chronoamperometric curve fitting in (a) dark and (b) light conditions.

The obtained values of τ are approximately 3.6 and 6 s in the light and dark conditions, respectively. The sample has the least transient current decay time in the light condition, indicating fast charge carrier dynamics. A shorter transient current decay time suggests that the material's charge carriers (electrons, holes, or ions) respond quickly to changes in the surrounding environment [293]. The observed fast charge dynamics in the light condition lead to increased photocurrent density, which aligns with our cyclic voltammetry results. However, there may be the possibility that the photogenerated electrons can be reduced from CuO to

Cu_2O. Still, our XRD and XPS results confirm the formation of pure and crystalline CuO NPs. It can be seen from the chronoamperometric results that after initial perturbation, the photocurrent density is stable. No degradation is observed in the sample during the reaction, which suggests that CuO can be used for long-term reactions.

5.4 Conclusion

In summary, CuO NPs were synthesized via a simple and inexpensive hydrothermal method, and their structural, optical, photoelectrochemical, and thermal properties were investigated at room temperature in dark and light conditions. XRD images and Rietveld refinement of the sample revealed the crystalline monoclinic structure of CuO. TEM and SAED images show the formation of crystalline quasi-spherical shaped nanoparticles. UV-visible spectra show that the sample is highly light-absorptive and exhibits a direct bandgap of 1.37 eV, which is suitable for HER activity and, hence, for hydrogen production. The low Urbach energy represents the lower structural disorder in the sample. A maximum specific capacitance of 36.62 F/g at 50 mV/s was observed in light conditions from the photoelectrochemical measurements. It is worth noting that CuO NPs have shown excellent photoelectrochemical HER activity in light conditions. A remarkably high HER photocurrent density of -41.57 mA/cm^2 at -0.6 V versus RHE is achieved with an onset potential of 0.535 V. CuO is abundant in nature and is a cost-effective material. We can use it on a large scale as it is plentiful. Moreover, hydrothermal is an easy and versatile technique, and it is a feasible process because the optimizations can be done very easily to synthesize highly pure and crystalline nanoparticles. As a photocathode, CuO performs equally well under dark and light conditions. This indicates that CuO is highly effective as a catalyst even without light exposure.